We are IntechOpen,
the world's leading publisher of
Open Access books
Built by scientists, for scientists

6,900
Open access books available

185,000
International authors and editors

200M
Downloads

154
Countries delivered to

Our authors are among the

TOP 1%
most cited scientists

12.2%
Contributors from top 500 universities

CLARIVATE ANALYTICS
BOOK CITATION INDEX
INDEXED

WEB OF SCIENCE™

Selection of our books indexed in the Book Citation Index
in Web of Science™ Core Collection (BKCI)

Interested in publishing with us?
Contact book.department@intechopen.com

Monitoring the Contractile Properties of Optically Patterned Liquid Crystal Based Elastomers

Kokou D. (Honorat) Dorkenoo, Emel Sungur,
Hervé Bulou, Grégory Taupier and Alex Boeglin

Additional information is available at the end of the chapter

1. Introduction

Liquid crystal materials offer many opportunities for applications such as data storage [1], image processing [2], or optical modulators [3] calling for media that are sensitive to external stimuli . Today, they are considered to have great potential for the realization of so called "smart materials" through micro- to nano-scale patterning techniques. One interesting material in the flourishing group of smart materials is the Liquid Crystal Elastomer (LCE) which combines the properties of liquid crystals and polymers. An elastomer is formed by a weakly crosslinked network of polymers, which confers it a high elasticity. The polymer network has maximum entropy in his undistorted state, and as a result, it resists deformation [4]. As for liquid crystals, these are materials which present phases intermediate between crystalline and isotropic called mesophases, the molecules responsible for this property are named mesogens.

In this chapter, we will present our results on the optical microstructuring of a LCE and the monitoring of its elastic properties. The liquid crystal based elastomer can be considered as an artificial muscle material. The designation of artificial muscle is attributed to soft actuators which can have muscle like behavior. A muscle is in reality an energy converter which converts chemical energy to mechanical motion. The actuators are converters which accept different types of energy and deliver a mechanical quantity like a displacement, a tension, *etc.*. The LCEs can be considered as artificial muscles in the sense that they may present a distortion, for example a contraction/extension generated by the crystalline-isotropic phase transition. The possibility of using liquid crystal elastomers (LCE) as external stimuli driven size changing materials was predicted by de Gennes in 1997 [5]. Since then, different LCE materials showing reversible macroscopic shape changes under thermal [6][7] or optical [8] stimulations have been produced. Here, we explore the use of this contraction/extension property to create stimulable microsystems.

The LCE used in this study is a nematic thermotropic (sensitive to thermal stimuli) elastomer. A nematic elastomer can be described as crosslinked polymer chains with incorporated mesogens corresponding to rigid rod-like units which can order nematically. The average shape of the material is coupled to the molecular orientation order [4][9]: the nematic-isotropic phase transition results in the change of shape of the macroscopic sample. When the elastomer is judiciously prepared to obtain a monodomain sample [10], meaning that all the mesogens are oriented uniformly, the sample is elongated in the nematic phase where all the mesogens are parallel to each other, and has a contracted shape in the isotropic phase where the nematic order is lost.

First, we will show that advantage can be taken of the crosslinking properties of the material to inscribe refractive index modulations by optical means as in a common photoresist [11]. We present two approaches based respectively on one- and two-photon photopolymerization, that can be implemented using an optical microscopy setup. Such a method provides an accurate way to locally modify the properties of the material. Compared to its one-photon relative, the two-photon excitation mode will yield finer patterns because of its higher intrinsic spatial resolution. This technique relies on the fact that the simultaneous absorption of two low energy photons is equivalent to the absorption of a high energy photon with an energy equal to the sum of these two photons energy. The two-photon absorption (TPA) process is a quadratic phenomenon: the probability of the simultaneous absorption of two photon is not proportional to the photon flux as in the case for the linear absorption, but to the square of the flux. TPA is then significant only for high incident fluences. Thus, the use of ultra-short pulse lasers combined with microscopy techniques allows light-matter interaction to be confined within a micrometric volume around the focal point.

After the presentation of the microstructuring process, we will describe how the contractile properties of the material can be measured by detecting the thermally induced step size changes of an inscribed grating. Finally, these results will be interpreted with the help of Molecular Dynamics (MD) simulations. MD is a powerful tool to elucidate the structure and the behavior of the molecules. It has been used to simulate the behavior of polymers [12] and has proved its efficiency to describe the liquid crystalline phases [13], thus it also allows the description of elastomer behavior [14]. MD consists of a computational method which calculates time dependent atomic motions by applying the laws of classical mechanics. We have used a combination of Lennard-Jones and Gay-Berne potentials to represent the anisotropic mesogens and the calculations have been carried out in the Parrinello-Rahman-Nosé-Hoover ensemble.

2. Materials

2.1. Photopolymerizable liquid crystals

LCE are materials combining the elastic properties of the elastomers and the anisotropic properties of liquid crystals. They are formed by reticulated liquid crystalline polymers, which, in general, at low reticulation degrees, conserve the mesomorphic properties of the polymer before reticulation as well as the nature of the phases and the transition temperatures. These elastomers, when subjected to external stimuli like temperature or electromagnetic fields, can mimic the actions of muscles (contraction/extension). They are, thereby, considered

as artificial muscle materials. Different types of actuators have been developed using polymers as parent material, like for example polymer gels [15] [16] [17], conductive polymers [18] [19] [20], carbon nanotubes [21] [22] [23] [24] or dielectric elastomers [25]. Soft and highly flexible, the polymers are well adapted to be used as artificial muscle materials due to their high strength, deformation capabilities, and their capacity to keep intact their properties after several operating cycles. Recently, LCE took over the field of artificial muscles. They are robust and don't need any solvent to operate (unlike the gels or conductive polymers). The concept of LCE was proposed by P. G. de Gennes in 1975 [9]. In his studies on reticulated liquid crystal polymers, he mentioned the possibility of the material deformation without constraint. In 1981 Frinkelmann *et al.* have realized the first mesomorphic oriented side-chain LCE [26] and afterwards the first main-chain LCE was synthesized by Bergmann *et al.* [27]. Indeed, according to the insertion topology of the mesogen (liquid crystal phase-forming unit)
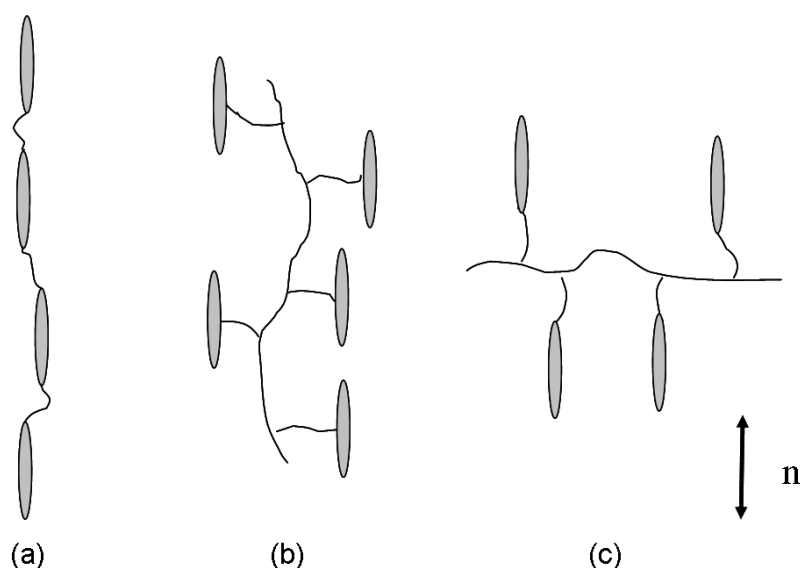

(a)   (b)   (c)

Figure 1. Schematic representation of different types of liquid crystal polymers: (a) main-chain, (b) side-chain side-on, (c) side-chain end-on.

in the elastomer, there exist two main families of LCEs: side-chain and main-chain elastomers. In the case of main-chain elastomers, the mesogens are directly integrated in the polymer chain, while in the case of side-chain elastomers, they are laterally attached to the polymer chain, either orthogonal to the chain, attached by one end (end on), or parallel to the chain, attached by the side (side on), as shown in figure 1.

Since the monomer used in this study is thermotropic, we will study the contraction properties of the resulting elastomer as a function of temperature. The studied elastomer is a nematic elastomer. The nematic phase is favored by the side-chain conformation. In nematic crystals, the mesogens have a random position but an orientational order: they are, on average, parallel to each other. This behavior is encouraged by the elongated form of these units. For a nematic crystal, the amount of order can be characterized by the order parameter P_2 defined as the average value of a second-order Legendre polynomial [28]:

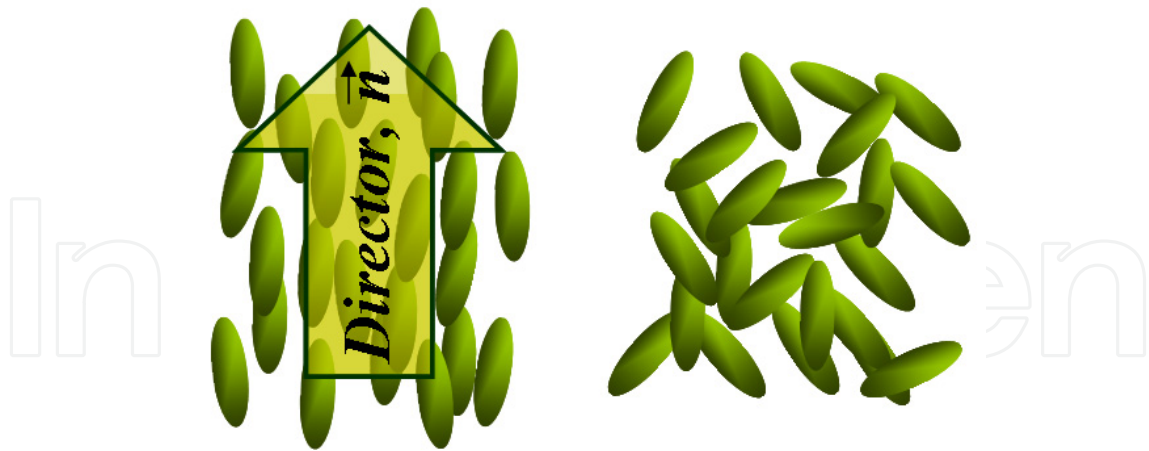$$P_2 = \frac{1}{2} < 3cos^2(\theta) - 1 >$$

(1)

Figure 2. Schematic representation of a liquid crystal in the nematic phase (left) and in the isotropic phase (right). The average orientation is represented by the nematic director **n**.

where θ corresponds to the angle between the long axis of the molecule and the nematic director. For a completely ordered phase $P_2=1$, while $P_2=0$ corresponds to a completely disordered phase (isotropic). The mesogens interact *via* long range dipolar or Van der Walls interactions. Below a given temperature, the interactions are sufficiently strong to orient the director axis and organize the system. Beyond this temperature, the preferential orientation of the mesogens is destroyed by the effect of entropy and an isotropic phase appears.
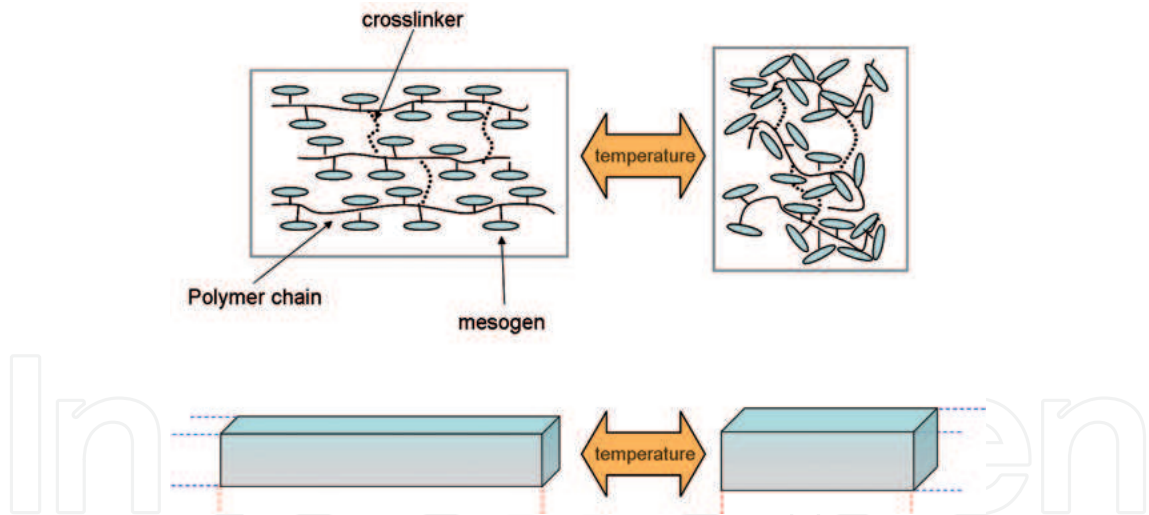

Figure 3. Contraction of a nematic thermotropic elastomer. Microscopic point of view (top), macroscopic point of view (bottom).

In the case of the elastomer, the mesomorphic properties (as the nature of phases of the initial monomers) are conserved. The mesogens attached to the sides of the main chain are free to move. During the nematic-isotropic phase transition the mesogens are disoriented and the main chain drag behind them. These microscopic form changes are transferred to the macroscopic sample. The destruction of the nematic order thus generates a contraction of the system along the mesogens alignment direction and an extension in the orthogonal directions as schematized in figure 3.

2.2. Elastomer thin film preparation

The precursor of the LCE used in this study is a mixture of three compounds: a liquid crystalline acrylate monomer, a crosslinker and an ultraviolet (UV) photoinitiator. The monomer whose structure is represented in figure 4 is the 4'-acryloyloxybutyl 2,5-(4'-butyloxybenzoyloxy)benzoate [29]. The part containing the aromatic chains is the rigid part of the monomer and the attached carbon chains correspond to soft parts. The photoinitiator is the 2-benzyl-2-(dimethylamine)-4' morpholinobutyrophenone (Irgacure 369) added at a concentration of 1 mol %, the crosslinker is the 1,6-hexanediol diacrylate at a concentration of 10 mol %. The elastomer is obtained by the photopolymerization of the monomers and the crosslinking of the polymeric chains. Let us recall that in the case
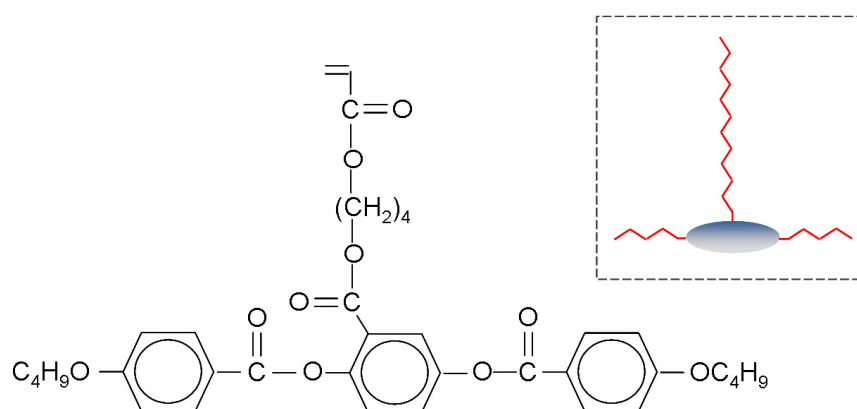

Figure 4. Chemical structure of the acrylate monomer. Inbox: schematics representation.

of a thermotropic nematic elastomer, the destruction of the nematic order by an increase in temperature will cause the contraction of the material along the nematic director. For the contraction to be maximum, the initial order parameter of the sample should be high. The samples were prepared in several micrometer thick glass cells filled by capillarity with the material in its isotropic phase (above 81.5 °C, the nematic-isotropic phase transition temperature). The cell surfaces were coated with rubbed poly-vinyl alcohol to insure the alignment of the liquid crystal moieties by guiding them during the filling process and allowing the production of a fully monodomain aligned sample. Thus the contraction can be unidirectional and along the original mesogens' alignment. To produce the elastomer the filled cell was slowly cooled down (1 °C/min) to the nematic phase (63 °C) conserving the alignment of the liquid crystal moieties. The elastomer film was then obtained by radical photopolymerization and photocrosslinking under UV light, fixing in this way the nematic alignment of the mesogens. The resulting monodomain elastomer film is named "Liquid Single Crystal Elastomer" (LSCE). The radical photopolymerization starts with the excitation of the photoinitiator Irgacure 369 which is a benzoyl type chromophore with a large absorbance and a high initiation efficiency in the range of 300-400 nm. The initiator generates a radical (a chemical species possessing one or several unpaired electrons in the outer shell) which can react with the monomer and form the macroradical which is also able to react with other monomers. The propagation of the polymerization proceeds by successive addition of monomers to this macro-radical. The monomers are bound to each other by the $CH=CH_2$ groups located at the extremities of the molecules. It is the breaking of the double bond that

allows the bonding between monomers. The polymerization takes place in such a way as to produce a form of "sheathing" of mesogen around the principal chain, thus avoiding steric hindrance (see figure 5). The crosslinker present in the mixture helps to create a crosslinked network and the elastomer so obtained can be extracted from the cell.
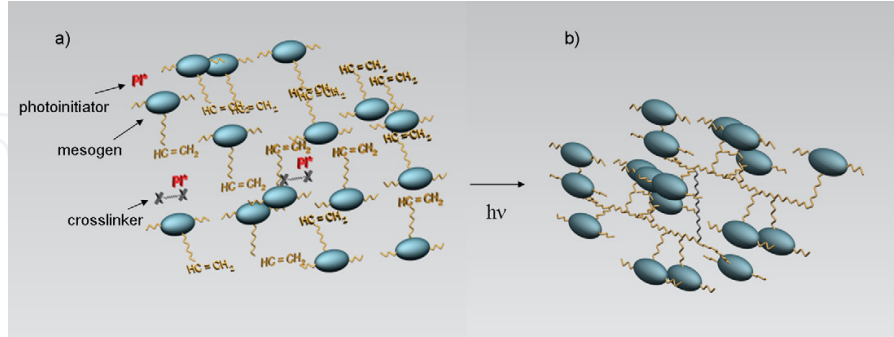

Figure 5. Elastomer formation by photopolymerization and photocrosslinking a) the initial mixture, b) the elastomer: the radical generated by the photoinitiator will activate the monomer which can then make a C-C bond with the following monomer; hence, the pôlymerization is accompanied by the formation of a sheathing around a main chain.

3. Experimental setup

Two different light sources were used to photo-structure the elastomers. We have used 365 nm UV light from an Argon Ion (Ar^+) laser to polymerize the mixture by one-photon photopolymerization or 780 nm infrared (IR) femtosecond laser pulse for two-photon photopolymerization. The advantage of two-photon absorption is the possibility to spatially confine the process by limiting the light-matter interaction to volumes which can be smaller than 1 μm^3. The probability of TPA is very low, its cross section is about 31 orders of magnitude lower than a one-photon absorption cross section. To be efficient TPA therefore necessitates a high density of photons. Thus, we have to spatially and temporally confine the photons. This can be achieved by combining the use of high numerical aperture objectives and ultra-short pulsed lasers such as titanium-sapphire lasers emitting in the near-IR region. When approaching the focal point of the objective, the photon density will sharply increase. The low probability TPA process will thus be automatically confined around this focal point in a volume called "voxel". If the sample is transparent to the IR radiation of the laser, but absorptive for the UV light, only the confined volume around the focal point will be excited, while the rest of the sample will remain transparent to the incident radiation. This microscopy technique is named "two-photon microscopy". Figure 6 presents a comparison between the excitation volumes in the case of conventional microscopy and two-photon microscopy. From the Rayleigh criterion, in optimal conditions, the radial resolution of a conventional microscope is given by the radius of the Airy disc:

$$r_{x,y} = \frac{0.61\lambda}{NA} \qquad (2)$$

In the case of two-photon microscopy, Webb *et al.* have proposed an estimation of the ω_{xy} and axial ω_z dimensions of the voxel [30]:
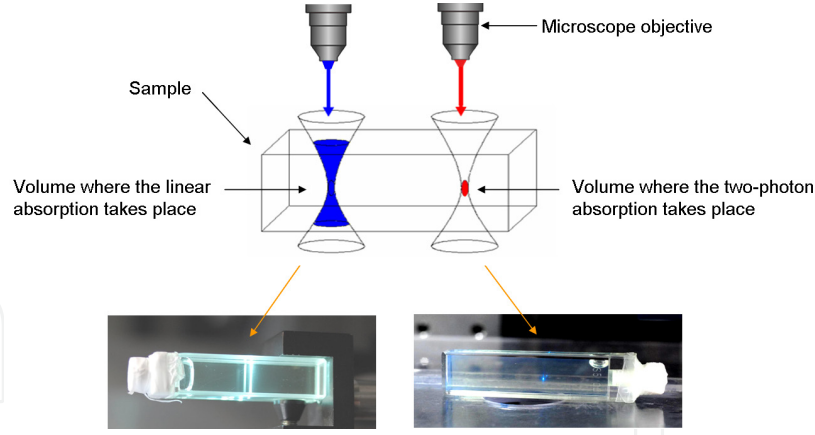
Figure 6. Comparison of the excitation volumes for the linear absorption (left) and two-photon absorption (right): in the linear case all the volume of the sample crossed by the beam is excited, in the case of two-photon absorption the excitation is confined to the voxel around the focal point. The photographies show the fluorescence signal emitted by the excited part of the sample.

$$\omega_{xy} = \begin{cases} \dfrac{0.32\lambda}{\sqrt{2}\mathrm{ON}} & \text{if ON} \leq 0.7 \\[3ex] \dfrac{0.325\lambda}{\sqrt{2}\mathrm{ON}^{0.91}} & \text{if ON} > 0.7 \end{cases} \quad \text{and} \quad \omega_z = \frac{0.532\lambda}{\sqrt{2}} \left(\frac{1}{n - \sqrt{n^2 - \mathrm{ON}^2}} \right) \quad (3)$$

The excitation is given by:

$$V_{2photon} = \pi^{3/2}\omega_{xy}^2\omega_z \quad (4)$$

The experimental setup used for the microstructurating and the realization of the elastomers is based on a confocal microscope. The cell containing the elastomer precursor mixture is placed on a heating plate mounted on a motorized stage that can execute computer-controlled 3D translations along the X, Y, and Z axes. The observation is done by reflection with a CCD camera. The sample is illuminated in transmission with a white light lamp; a filter is used to stop any UV photons. The sample is also placed between polarizers allowing the monitoring of isotropic and nematic zones through the polarization of transmitted light induced by the mesogen alignment. The photo-patterning of the desired structures is realized in the nematic phase by moving the sample under the focus of the objective with the translation stage.

4. Experimental results

4.1. Photostructuration of the material

We have first studied the creation of a patterned elastomer by photopolymerization initiated by linear or two-photon absorption. Different sets of experiments have been performed depending on the sample alignment state (using treated or untreated glass cells) and the excitation source (UV or IR light). The first set of experiments was made using UV excitation (Argon laser, λ= 365 nm, power = 8 μW, objective N.A = 0.45) and a non-aligned nematic monomer sample. In a first step the photopolymerizable mixture was introduced in an untreated cell. Then the cell was heated beyond the isotropic-nematic
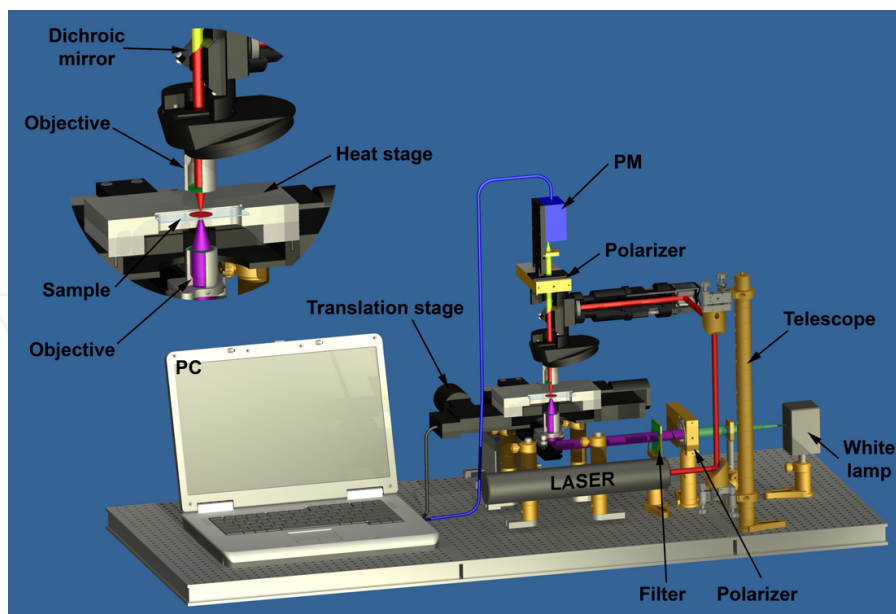
Figure 7. Experimental setup.

phase transition temperature (> 81.5 °C) for the mixture initially in the form of a powder to liquefy and penetrate by capillarity. The mixture was then cooled down until the nematic phase could form (63 °C). A shape representing the capital letter E has been patterned by photopolymerization with the focused UV beam using the translation stage with a displacement velocity of 200 μm/s. The resulting polymerized and crosslinked part draws the letter "E" as can be seen in figure 8(a). The second set of experiments was performed under the same conditions as described above, except that an aligned nematic monomer sample was used figure 3(b). This polymerization was also successful. The polymerized letter "E" presents thinner (30 μm) and smoother lines than those obtained for the non-aligned sample (50-60 μm). The patterned lines are undistorted in the aligned sample. Therefore, using aligned nematic samples results in considerably improved micro-pattern formation. In the third set of experiments performed again on aligned samples, the IR source (Ti:Sa laser, pulses duration = 100 fs, repetition rate = 80 MHz , λ= 780 nm, power = 500 mW, objective N.A = 0.45) was used instead of the Argon laser. The results presented in figure 3(c) show that such two-photon excitation processes produce a smooth pattern with even thinner lines measuring 5 to 10 μm across. The high resolution achieved in this case is indeed better than UV illumination.

Figure 8. Letter "E" patterns (a) by one-photon photopolymerization (UV irradiation) in a nonaligned sample, (b) by one-photon photopolymerization (UV irradiation) in an aligned sample, (c) by two-photon photopolymerization (IR irradiation) in an aligned sample. The nematic director orientation is indicated by the arrow.

4.2. Obtaining the thermo-active elastomer

In order to stabilize the patterns, a post-photopolymerization of the whole sample can be performed using UV light of weak intensity. Under these conditions, the pattern written by photopolymerization using a high intensity beam is preserved as it can be seen on figure 9. The resulting rubber-like film is then removed from the cell and placed on a heating plate to observe the shape changes as a function of temperature. Figure 10 represents the heating of an elastomer with an inscribed grating of 170 μm step size. The elastomer lies on a film of glycerol oil to minimize the constraints during the contraction. By heating this sample up from room temperature to 120 °C, a clear deformation of the film is observed in the direction of the mesogen alignment. An elastomer with a circular pattern was also produced to highlight the
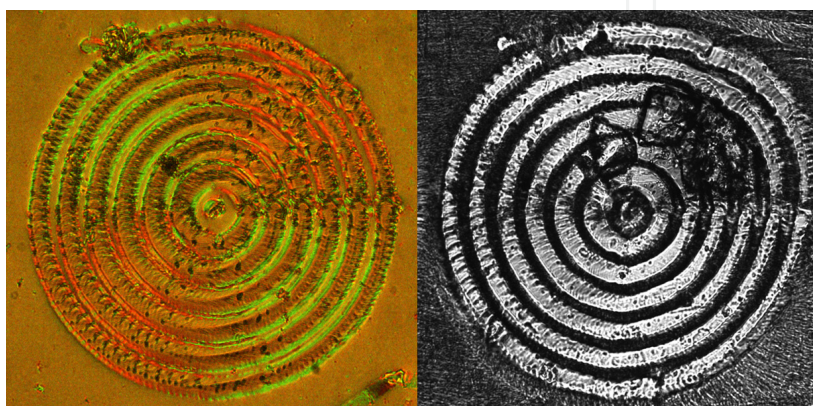

Figure 9. Concentric figure inscribed by photopolymerization before postpolymerization of the whole sample (left), after postpolymerization (right), the zone surrounding the pattern has a weaker polymerization degree.
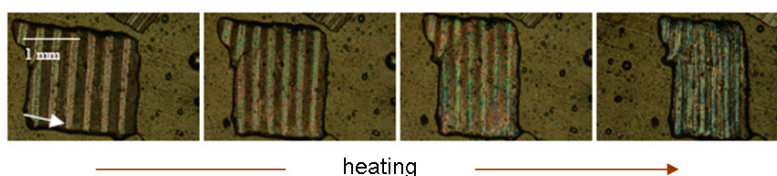
Figure 10. Contraction of a 20 μm thick elastomer as a function of temperature (from 60 °C to 120 °C).

uniaxial contraction and the reversible aspect of the phenomenon as can be seen in figure 11.

5. Discussion

5.1. Contraction properties

Direct observation of the micropatterned elastomer's contraction can be readily achieved by optical microscopy. Figure 12 shows the temperature dependent deformation of the concentric pattern inscribed in a 13 μm thick film of elastomer. The value of the width perpendicular to the nematic director (denoted a) shows a small variation (less than 2% of extension) whereas the perpendicular direction (denoted b) experiences about 17% of contraction. This demonstrates that the shape change consists mostly in a contraction along the nematic director and proves that a well aligned monodomain sample was achieved. This contraction factor varies with the sample thickness. About 50% contraction is observed in 30 μm thick samples

Figure 11. Deformation of concentric cercle patterned in the elastomer as a function of temperature. "a" and "b" correspond to the resulting ellipse axis, "b" is in the mesogen alignment direction.

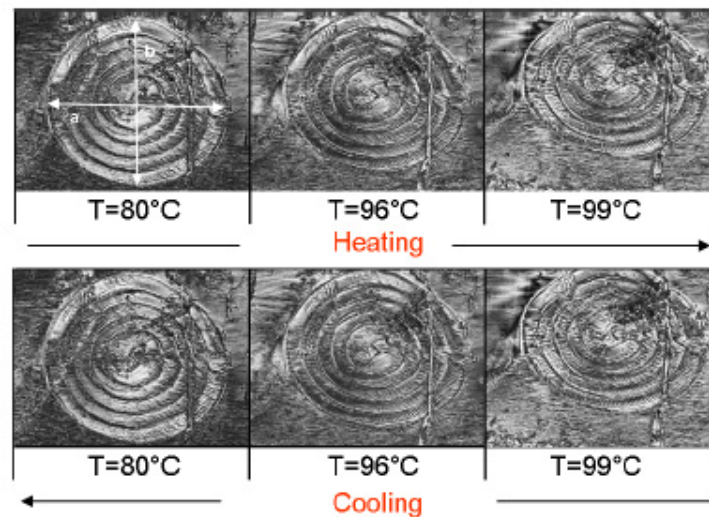but as the thickness decreases, the contraction drops to about 30% for 20 μm thick samples and to about 17 % for 13 μm thick samples. This behavior can be attributed to mechanical stress. Indeed, the size of the artificial muscle with respect to the surface of adhesion is larger for a thick film than for a thin film. The contraction forces thus become prevalent (as the samples become thicker) over the constrains resulting from the friction of the film on its substrate. It is noteworthy that no dependency of the rate of contraction on the pattern structure has been observed, suggesting that any diffraction element can be inscribed without altering the physical properties of the material. The contraction of the elastomer starts around 90 °C. It stops when the phase becomes isotropic, towards 100 °C. Both of these temperatures are higher than the phase transition temperatures of the initial liquid crystal which is 81.5 °C. The mesogens being free to move within the elastomer, the thermal characteristics of the mesophases should be preserved. This is, however, only partially true since the mesogens are not completely decoupled from the main chain. However it is reasonable to assume that the longer the spacer, the higher the degree of this decoupling. This aspect may thus bear on the phase transition temperature but there is no doubt that the primary cause behind the observed contraction temperatures lies with the fact that the response of the material to the drop in nematic order is not immediate. Contraction will only occur once the degree of disorientation of the mesogens reaches levels that are enough to overcome the frictional forces between the elastomer and its substrate. In addition, with the monitoring technique that is being put to use, the contraction becomes only apparent beyond a certain level. All this may be the origin of the gap between the phase transition temperature and the temperature at which contraction is being observed.

5.2. Diffraction properties

The contraction of the material can be monitored indirectly by the observation of the diffraction pattern proceeding from a grating inscribed in the elastomer. Temperature induced contraction of the material will result in a change in the grating period which will modify the diffraction pattern. We present the study of the diffraction pattern obtained for a 13
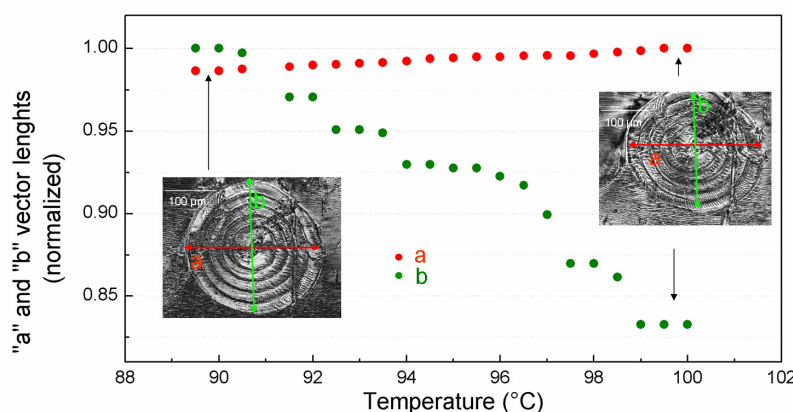
Figure 12. Deformation of concentric circles separated by 25 μm as a function of temperature; "a" and "b" correspond to the axes of the resulting ellipse. The insets show the samples at the temperatures indicated by the arrows.

μm thick sample with a 30 μm period linear grating using a linearly polarized He-Ne laser beam at 633nm. Before testing the properties of the obtained gratings, we have examined
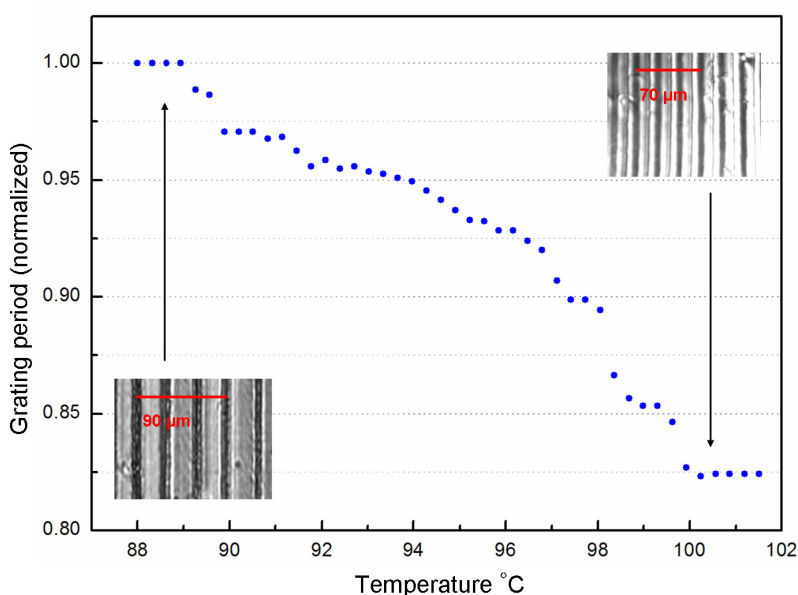
Figure 13. Grating step as a function of temperature, in the case of a 13 m thick sample. The internal figures represent the grating at the corresponding temperatures.

the surface of the elastomer with a profilometer. In some cases when the sample is removed from the cell, its surface exhibits ridges corresponding to the grating. Such observations are commonly made in photopolymerization experiments [31]. The surface corrugation comes from the relaxation of the mechanical stresses introduced by the cross-linking process and which have been maintained by the glass plates. These ondulations are not observed in two-photon photopolymerized samples where the patterns are much thinner and inscribed inside the volume of the elastomer. In the cases where inscribed gratings led to surface ridges, we have checked that the addition of a compensating liquid did not modify the diffraction properties. Thus we may pretend that we are dealing with refractive index gratings. Index

inhomogeneity stems from spatial variations in material density between parts that have been strongly polimerized and the remainder of the sample which has only been subjected to a light post-polymerization. The diffraction regime is indicated by the Klein-Cook parameter $Q = 2\pi\lambda_0 L/\Lambda^2 n_0$, where L is the grating thickness, λ_0 is the vacuum wavelength of light, Λ is the grating step size, and n_0 is the mean refractive index. High values of Q (Q>10) correspond to the Brag regime while low values (Q<1) correspond to the Raman-Nath regime. One usually ascribes the Bragg regime, with essentialy only one diffracted wave being produced, to gratings that are thick with respect to step size and the Raman-Nath regime, with several diffracted waves being produced, to thin gratings. In the case of a grating with a step size of 30 μm and a thickness of 13 μm yielding the diffraction pattern shown in figure 14, the Q parameter is about 0.4, placing the diffraction in the Raman-Nath regime as demonstrated by the multiple order diffraction pattern. Figure 15 shows the variation of the angle of diffraction for the +1 order as a function of temperature. It clearly demonstrates the decrease
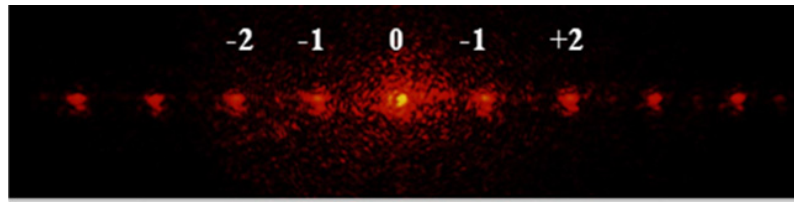

Figure 14. Diffraction figure of 30m step gratings inscribed into the elastomer.

of the grating step with the temperature rise stemming from the unidirectional contraction accompanying the nematic/isotropic transition. In figure 15, the black dots correspond to measurements of the diffraction angle, while the red dots represent values calculated following the diffraction grating formula from the data shown in figure 13 for the 13 μm thick sample. The agreement between both sets of data shows the consistency between the grating period and the diffraction angle measurements (discrepancies between data points may come from the fact that they have been gathered over several heating cycles). In conclusion, the contraction induced by the temperature is easily monitored by the widening of the diffraction figure. This allows a feedback on the deformation of the material through direct monitoring of the resulting diffraction.

Since we work with a cross-linked polymer, the contraction/extension process will affect all three directions in space. The initial homogeneous nematic order makes the film behave as a biaxial material with an optical axis oriented along the nematic director. Thus, the material may change the polarization state of the light upon diffraction. To illustrate the birefringence properties of the gratings, we have measured the diffraction efficiency dependence on the orientation of the incident linear polarization. The resulting angular distribution for the polarization of the diffracted light is presented in figure 16b. Here, the simplest configuration is adopted: the incident beam is normal to the surface and its polarization is linear. As one can see in figure 16a, the diffraction efficiency is higher when the direction of the polarization of the incident beam and the grating vector are parallel. The diffracted light intensity has been fitted by :

$$I = \eta_\parallel \cos^2 \phi + \eta_\perp \sin^2 \phi \tag{5}$$

where the angle ϕ corresponds to the rotation of the polarisation and I is the light intensity of the first diffracted order. Thus we can determine the parallel and the perpendicular diffraction
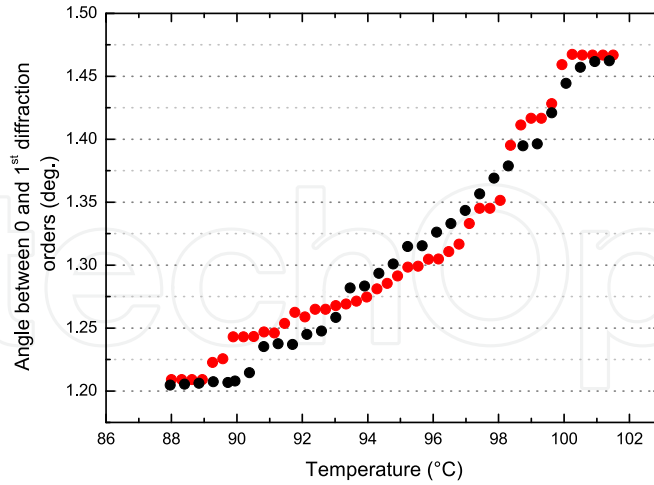
Figure 15. Variation of the first order diffraction angle of a 30 μm period grating as a function of temperature: black dots are the measured diffraction angles, red dots are calculated from the data on figure 13.

efficiencies which amount respectively to $\eta_{\parallel} = 1$ and $\eta_{\perp} = 0.53$.

In the case of figure 16b the incident beam polarization is at 45° of the grating vector. This time a light intensity dependence on the rotation of an analyzer placed after the sample is observed. Equation (6) represents the theoretical function which will fit the intensity of light measured after the analyser.

$$I = \left| \sqrt{\eta_{\parallel}} \, \cos\phi \, \frac{\sqrt{2}}{2} \, e^{(i\,\psi/2)} + \sqrt{\eta_{\perp}} \, \sin\phi \, \frac{\sqrt{2}}{2} \, e^{(-i\,\psi/2)} \right|^2 \tag{6}$$

For $\eta_{\parallel}$ and $\eta_{\perp}$ we take the diffraction efficiencies determined in figure 16a. The phase difference ψ is introduced by the birefringence and ϕ is the analyser angle. Figure 16b represents experimental data and the fits for the zero and the first diffraction orders. We observe the slight depolarization of the zero order due to the intrinsic material birefringence when comparing it to the polarization of the incident beam added as a reference. Diffraction order +1 shows a more elliptic polarization and a rotation of the major axis. Calculations give a rotation of 29.7^o. We have been able to make these observations on various samples and are led to consider that this behavior finds its origin in two simultaneous effects. The first is obviously the birefringence of the material which introduces a phase difference between the parallel and the perpendicular components of the field and causes the depolarization of the diffracted beam. The other effect originates in the diffraction grating: the refractive index modulation seen by the beam is different for the direction along the grating vector and for the perpendicular to it. Therefore, the diffraction efficiencies for polarizations along these two directions are not identical. Hence, the decomposition of the polarization of the diffracted beam along these directions will be different with respect to that of the incoming light. As temperature increases, the material tends to the isotropic configuration and the observed birefringence tends to get attenuated.
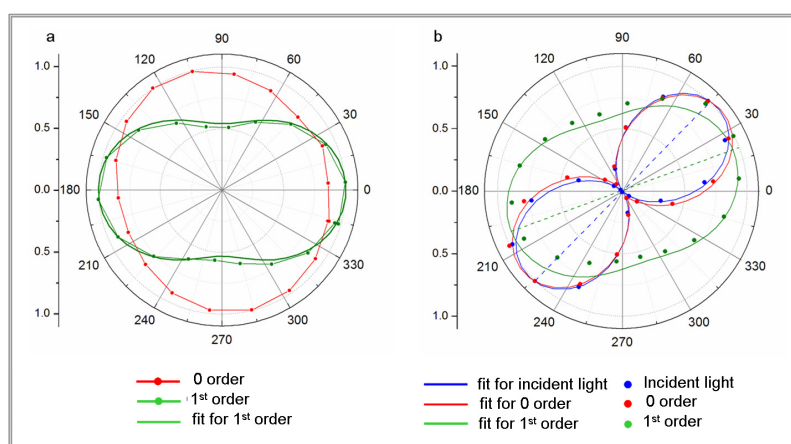
Figure 16. Polarization of diffracted light. (a) zero- and first-order diffraction intensities versus incident beam linear polarization orientation. (b) Incident beam, zero-, and first-order diffraction intensities versus analyzer angle. The direction of the grating vector corresponds to the angle zero.

5.3. Molecular dynamics simulations

Molecular dynamics (MD) simulations are a powerful tool for understanding the properties of a sample in terms of molecular collective phenomena. We used classical MD method to simulate the contraction of the elastomer. First, the monomer molecules composed of 95 atoms was fully optimized by the density functional theory (DFT). The chosen functional was B3LYP, a hybrid functional obtained by linear combination of exchange-correlation energy functionals (Local-density approximations LDA, Generalized gradient approximations GGA) and the Hatree-Fock exchange [32]. The orbital basis set was the contracted Gaussian 6-311** set. All calculations were carried out with NWChem [33], executed on the IBM Power 6 at the "Institut du Développement et des Ressources en Informatique Scientifique" of Orsay. The obtained minimum energy configuration is represented in figure 17. This model presents a dipole localized on the mesogen corresponding to the aromatic core. This will allow
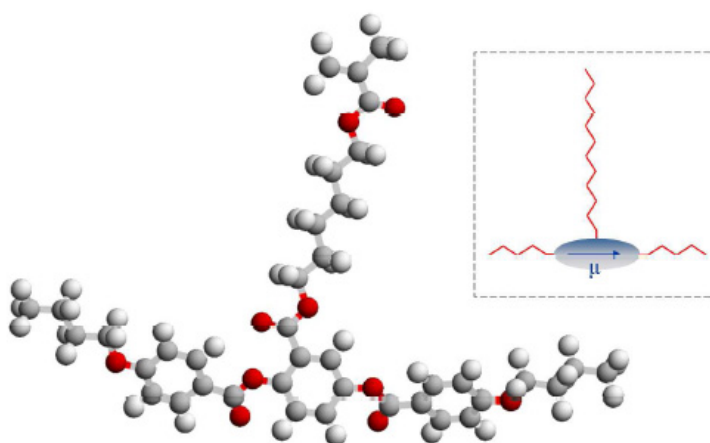
Figure 17. Model of the monomer: minimum energy configuration. Inbox: schematical representation; a dipole is localized on the rigid mesogenic site corresponding to the aromatic core.

dipole-dipole interactions between the monomers. Then to simulate the contraction of the elastomer resulting from the collective behavior of the monomers the interaction between pairs of anisotropic rigid mesogenic sites was modeled using Gay-Berne (GB) potential. The Gay-Berne potential corresponds to a modified form of Lennard-Jones potential which can be easily adjusted to modify the shape of the studied system [34]. In that sense it has proven its efficiency to model mesogenic systems [35][36][37].

The force field modeling intra and inter-molecular contribution to the interaction energy is given by the following expression:

$$
\begin{aligned}
U = {} & \sum_{i=1}^{N_{angles}} \frac{k_i^{ang}}{2} \left(\theta_i - \theta_i^0\right)^2 \\
& + \sum_{i=1}^{N_{GB}} \frac{k_i^{GB}}{2} \left(v_i - v_i^0\right)^2 + \\
& + \sum_{i=1}^{N_{dihedrals}} \left(a_{i,1}\left(1 + \cos\phi_i\right) + a_{i,2}\left(1 - \cos 2\phi_i\right) + a_{i,3}\left(1 + \cos 3\phi_i\right)\right) \\
& + \sum_{i=1}^{N_{LJ}} \sum_{j>i}^{N_{LJ}} U_{LJ} \\
& + \sum_{i=1}^{N_{LJ}} \sum_{j=1}^{N_{GB}} U_{LJ/GB} \\
& + \sum_{i=1}^{N_{GB}} \sum_{j>i}^{N_{GB}} U_{GB}
\end{aligned}
\tag{7}
$$

where N_{angles}, $N_{dihedrals}$, N_{GB}, N_{LJ}, are respectively the angles number of the dihedral angles of the numbers, and the number of GB and LJ sites numbers. The variations in dihedral angles ϕ, which represent torsions, are modeled by a truncated Fourier series ($a_{i,1,2,3}$ coefficients). The alkyne groups of the chain are condensed into single atom sites and represented as spheres. All the chain segment parameters are modeled by resorting to universal force field [38]. U_{LJ}, U_{GB} et $U_{LJ/GB}$ are respectively Lennard-Jones, Gay-Berne and the mixte Lennard-Jones/Gay-Berne potentials. Bond lengths between the mesogen and the flexible chains were set from *ab initio* results. They are 1.495 Å for the C-mesogen bond and 1.353 Å for the O-mesogen bond. The bond lengths between chain segments and GB unit were constrained by using the SHAKE procedure [39] during molecular dynamics calculations. v_i corresponds to the angle between the long axis of the GB site and the bond between this site and the adjacent one. v_i^0 is the equilibrium value and k_i^{GB} corresponds to the force constant given by DFT calculations ($v_{GBC}^0 = 112.62\,°\text{C}$ and $k_{GBC}^0 = 6.521\,\text{eV/rad}^2$).

For a separation distance of r_{ij} between two particles, the standard LJ potential is written as:

$$
U_{LJ} = \sum_i \sum_{j>i} 4\epsilon_{ij} \left(\left(\frac{\sigma_{ij}^{(0)}}{r_{ij} - \sigma_{ij} + \sigma_{ij}^{(0)}}\right)^{12} - \left(\frac{\sigma_{ij}^{(0)}}{r_{ij} - \sigma_{ij} + \sigma_{ij}^{(0)}}\right)^6\right)
\tag{8}
$$
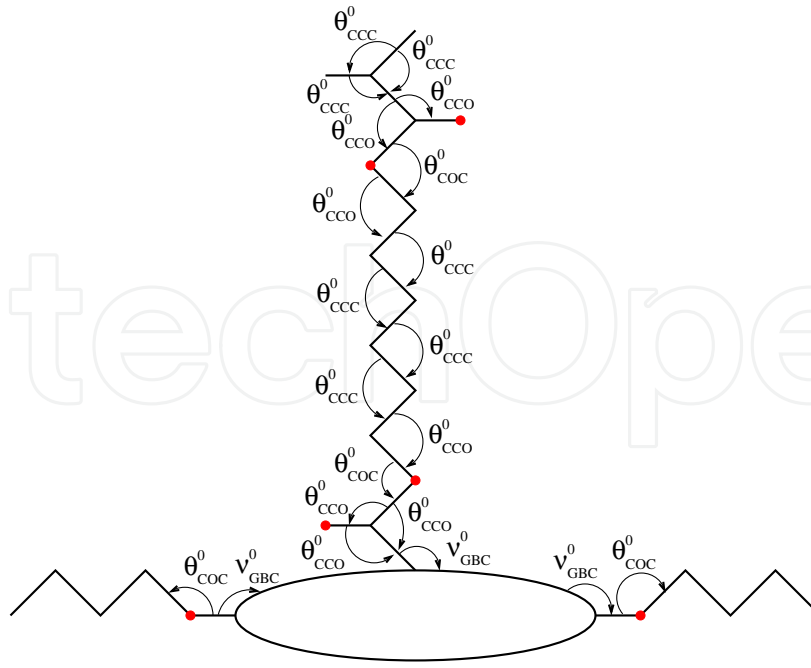
Figure 18. Representation of different bonding angles.

where ϵ_{ij} corresponds to the energy well depth, σ_{ij} is the contact parameter, it corresponds to the separation distance at which the inter-particle potential is zero.

U_{GB} represents the orientation dependent interaction energy for two GB particles:

$$U_{GB} = \sum_i \sum_{j>i} 4\epsilon_{ij}\left(\hat{\mu}_i, \hat{\mu}_j, \hat{r}_{ij}\right) \left(\left(\frac{\sigma_{ij}^{(0)}}{r_{ij} - \sigma_{ij}\left(\hat{\mu}_i, \hat{\mu}_j, \hat{r}_{ij}\right) + \sigma_{ij}^{(0)}} \right)^{12} \right.$$
$$\left. - \left(\frac{\sigma_{ij}^{(0)}}{r_{ij} - \sigma_{ij}\left(\hat{\mu}_i, \hat{\mu}_j, \hat{r}_{ij}\right) + \sigma_{ij}^{(0)}} \right)^{6} \right) \tag{9}$$

where $\hat{\mu}_i$ and $\hat{\mu}_j$ are unitary vectors along the molecular axis of GB particles, ϵ_{ij} and σ_{ij} correspond respectively to the energy well depth and the contact parameter depending on the relative orientation of the particles. These terms are defined as [36] [40]:

$$\sigma_{ij}\left(\hat{\mu}_i, \hat{\mu}_j, \hat{r}_{ij}\right) = \frac{\sigma_{ij}^{(0)}}{\sqrt{1 - \frac{\chi}{2}\left[\frac{\left(\hat{\mu}_i\cdot\hat{r}_{ij}+\hat{\mu}_j\cdot\hat{r}_{ij}\right)^2}{1+\chi\left(\hat{\mu}_i\cdot\hat{\mu}_j\right)} + \frac{\left(\hat{\mu}_i\cdot\hat{r}_{ij}-\hat{\mu}_j\cdot\hat{r}_{ij}\right)^2}{1-\chi\left(\hat{\mu}_i\cdot\hat{\mu}_j\right)} \right]}} \tag{10}$$

$$\epsilon_{ij}\left(\hat{\mu}_i, \hat{\mu}_j, \hat{r}_{ij}\right) = \epsilon_0 \epsilon_1^\gamma\left(\hat{\mu}_i, \hat{\mu}_j, \hat{r}_{ij}\right) \epsilon_2^\nu\left(\hat{\mu}_i, \hat{\mu}_j\right) \tag{11}$$

$$\epsilon_1\left(\hat{\mu}_i, \hat{\mu}_j, \hat{r}_{ij}\right) = 1 - \frac{\chi'}{2}\left[\frac{\left(\hat{\mu}_i\cdot\hat{r}_{ij}+\hat{\mu}_j\cdot\hat{r}_{ij}\right)^2}{1+\chi'\left(\hat{\mu}_i\cdot\hat{\mu}_j\right)} + \frac{\left(\hat{\mu}_i\cdot\hat{r}_{ij}-\hat{\mu}_j\cdot\hat{r}_{ij}\right)^2}{1-\chi'\left(\hat{\mu}_i\cdot\hat{\mu}_j\right)} \right] \tag{12}$$

$$\epsilon_2\left(\hat{\mu}_i, \hat{\mu}_j\right) = \frac{1}{\sqrt{1 - \chi^2\left(\hat{\mu}_i \cdot \hat{\mu}_j\right)^2}} \tag{13}$$

$$\chi = \frac{(\sigma_E/\sigma_s)^2 - 1}{(\sigma_E/\sigma_s)^2 + 1}$$

$$\chi' = \frac{1 - (\epsilon_E/\epsilon_s)^{1/\gamma}}{1 + (\epsilon_E/\epsilon_s)^{1/\gamma}} \tag{14}$$

with σ_E and σ_S corresponding to the contact parameter along the GB particle length and width and ϵ_E and ϵ_S corresponding to the energy well depth for two GB particles with an "end to end" and a "side by side". r_{ij} is the distance between the two particles i and j, $\hat{r}_{ij}$ corresponds to the unitary vector along $\vec{r}_{ij}$, $\hat{\mu}_i$ and $\hat{\mu}_j$ are unitary vectors along the molecular axis of the particles i and j. γ and ν are adjustable parameters which were set to their canonical values of 1.0 and 2.0, respectively. The ratio was σ_E/σ_s=3.46 and ϵ_0=21.2 meV.

$U_{LJ/GB}$ corresponds to the potential representing the mixte interaction between LJ and GB sites [40]:

$$U_{GB/LJ} = \sum_i \sum_j 4\epsilon_{ij}\left(\hat{\mu}_i, \hat{r}_{ij}\right) \left(\left(\frac{\sigma_{ij}^{(0)}}{r_{ij} - \sigma_{ij}\left(\hat{\mu}_i, \hat{r}_{ij}\right) + \sigma_{ij}^{(0)}}\right)^{12} \right.$$

$$\left. - \left(\frac{\sigma_{ij}^{(0)}}{r_{ij} - \sigma_{ij}\left(\hat{\mu}_i, \hat{r}_{ij}\right) + \sigma_{ij}^{(0)}}\right)^6 \right) \tag{15}$$

We have considered the molecular dynamics in a modified isothermal-isobaric (NPT) ensemble to allow an anisotropic deformation of the simulation cell. The ensemble used is the Parrinello-Rahman-Nosé-Hoover ensemble based on the H_{PRNH} Hamiltonian [41] [42] [43]. Thanks to the introduction of a thermostat and a barostat, this ensemble allows to control the temperature and the constraints acting on the simulation cell. It allows the study of anisotropic deformation of a system as a function of temperature. It is in that sense well adapted to the study of systems containing liquid crystal molecules. The H_{PRNH} Hamiltonian is given by:

$$H_{PRNH} = \frac{1}{2}\sum_{i=1}^{N}\frac{1}{m_i}\vec{P}_i^T \bar{\bar{G}} \vec{P}_i + U \tag{16}$$

$$+ \frac{1}{2Q}P_\eta^2 + gk_B T\eta$$

$$+ \frac{1}{2W}Tr\left(\bar{\bar{P}}_h^T \bar{\bar{P}}_h\right) + P_{ext}\Delta\bar{\bar{h}}$$

$$+ \frac{1}{2}\sum_{i=1}^{N_{GB}}\frac{1}{m_{\vec{\rho}_i}}\vec{P}_{\vec{\rho}_i}^T \vec{P}_{\vec{\rho}_i} \tag{17}$$

with $\bar{\bar{G}} = \bar{\bar{h}}^T\bar{\bar{h}}$.

$\bar{\bar{h}}$ is the matrix containing the dimensions of the unit cell L_x, L_y and L_z, $\bar{\bar{P}}_h$ is the conjugated moment and together they form the dynamical variables of the system relating to the control of

the constraints acting on the simulation cell. W is a fictive mass which allows the adjustments of the barostat's reactions to the constraints' changes. m_i is the i particle mass. $\vec{P}_i$ is its momentum:

$$\vec{P}_i = m_i \frac{d\vec{S}_i}{dt} \tag{18}$$

where $\vec{S}_i$ is the reduced position of the particle in the simulation cell

$$\vec{S}_i = \bar{\bar{h}}^{-1} \vec{q}_i \tag{19}$$

and $\vec{q}_i$ corresponds to the absolute position. η and P_η are dynamical variables relating to the control of the temperature. Q is a fictive mass which allows to adjust the thermostat reactions to temperature changes in the system. $\vec{\rho}$ and $\vec{P}_{\vec{\rho}}$ are dynamical variables relating to the long range interactions between GB sites. $m_{\vec{\rho}}$ is the mass relating to this type of interactions and controlling its dynamics.

The forces acting on the system are obtained by deriving the field U. The system's deformations are obtained by integrating the equations of motion using Beeman's algorithme [44]:

$$\vec{S}_i(t+\delta t) = \vec{S}_i(t) + \frac{\delta t}{m_i}\vec{P}_i(t) + \frac{\delta^2}{6m_i}\left(4\frac{d\vec{P}_i(t)}{dt} - \frac{d\vec{P}_i(t-\delta t)}{dt}\right) \tag{20}$$

$$\vec{P}_i(t+\delta t) = \vec{P}_i(t) + \frac{\delta t}{6}\left(5\frac{d\vec{P}_i(t)}{dt} + 2\frac{d\vec{P}_i(t+\delta t)}{dt} - \frac{d\vec{P}_i(t-\delta t)}{dt}\right) \tag{21}$$

$$\bar{\bar{h}}(t+\delta t) = \bar{\bar{h}}(t) + \frac{\delta t}{W}\bar{\bar{P}}_h(t) + \frac{\delta^2}{6W}\left(4\frac{d\bar{\bar{P}}_h(t)}{dt} - \frac{d\bar{\bar{P}}_h(t-\delta t)}{dt}\right) \tag{22}$$

$$\bar{\bar{P}}_h(t+\delta t) = \bar{\bar{P}}_h(t) + \frac{\delta t}{6}\left(5\frac{d\bar{\bar{P}}_h(t)}{dt} + 2\frac{d\bar{\bar{P}}_h(t+\delta t)}{dt} - \frac{d\bar{\bar{P}}_h(t-\delta t)}{dt}\right) \tag{23}$$

$$\eta(t+\delta t) = \eta(t) + \frac{\delta t}{Q}P_\eta(t) + \frac{\delta^2}{6Q}\left(4\frac{dP_\eta(t)}{dt} - \frac{dP_\eta(t-\delta t)}{dt}\right) \tag{24}$$

$$P_\eta(t+\delta t) = P_\eta(t) + \frac{\delta t}{6}\left(5\frac{dP_\eta(t)}{dt} + 2\frac{dP_\eta(t+\delta t)}{dt} - \frac{dP_\eta(t-\delta t)}{dt}\right) \tag{25}$$

$$\vec{\rho}_i(t+\delta t) = \vec{\rho}_i(t) + \frac{\delta t}{m_{\vec{\rho}_i}}\vec{P}_{\vec{\rho}_i}(t) + \frac{\delta t^2}{6m_{\vec{\rho}_i}}\left(4\frac{d\vec{P}_{\vec{\rho}_i}(t)}{dt} - \frac{d\vec{P}_{\vec{\rho}_i}(t-\delta t)}{dt}\right) \tag{26}$$

$$\vec{P}_{\vec{\rho}_i}(t+\delta t) = \vec{P}_{\vec{\rho}_i}(t) + \frac{\delta t}{6}\left(5\frac{d\vec{P}_{\vec{\rho}_i}(t)}{dt} + 2\frac{d\vec{P}_{\vec{\rho}_i}(t+\delta t)}{dt} - \frac{d\vec{P}_{\vec{\rho}_i}(t-\delta t)}{dt}\right) \tag{27}$$

An autocoherent process is necessary to calculate the conjugated moments. The time derivatives of the moments are calculated with the Parrinello-Rahman-Nosé-Hoover

Hamiltonian.

$$\frac{d\vec{P}_i}{dt} = -\frac{1}{Q}P_\eta \vec{P}_i - \bar{\bar{G}}^{-1}\frac{d\bar{\bar{G}}}{dt}\vec{P}_i - \bar{\bar{h}}^{-1}.\vec{\nabla}_{\vec{q}_i}U \tag{28}$$

$$\frac{d\vec{P}_{\vec{\rho}_i}}{dt} = -\vec{\nabla}_{\vec{\rho}_i}U \tag{29}$$

$$\frac{dP_\eta}{dt} = \sum_{i=1}^{N}\frac{1}{m_i}\vec{P}_i^T\bar{\bar{G}}\vec{P}_i + \frac{1}{W}Tr\left(\bar{\bar{P}}_h^T\bar{\bar{P}}_h\right) - gk_BT \tag{30}$$

$$\frac{dP_{h,\alpha\beta}}{dt} = -\frac{1}{Q}P_\eta P_{h,\alpha\beta} + \frac{1}{2}\sum_{i=1}^{N}\frac{1}{m_i}\vec{P}_i^T\frac{d\bar{\bar{G}}}{dh_{\alpha\beta}}\vec{P}_i - \frac{\partial U}{\partial h_{\alpha\beta}} - P_{ext}\frac{\partial\Delta\bar{\bar{h}}}{\partial h_{\alpha\beta}} \tag{31}$$

$$\alpha,\beta = x,y,z$$

$$
\begin{aligned}
\frac{\partial U}{\partial\mu_{k,\alpha}} = \frac{1}{\mu_k}\sum_{i\neq k}^{N_{GB}}&\left\{(\hat{\mu}_{i,\alpha} - \hat{\mu}_{k,\alpha}\hat{\mu}_k\cdot\hat{\mu}_i)\cdot\left[\nu\chi^2\varphi_{ki}\Omega_{ki}^2\hat{\mu}_i\cdot\hat{\mu}_k\right.\right.\\
&+ \mu\chi'^2\frac{\varphi_{ki}}{\Theta_{ki}}\left[\frac{(\hat{\mu}_k\cdot\hat{r}_{ki} + \hat{\mu}_i\cdot\hat{r}_{ki})^2}{(1+\chi'\hat{\mu}_k\cdot\hat{\mu}_i)^2} - \frac{(\hat{\mu}_k\cdot\hat{r}_{ki} - \hat{\mu}_i\cdot\hat{r}_{ki})^2}{(1-\chi'\hat{\mu}_k\cdot\hat{\mu}_i)^2}\right]\\
&- \frac{\chi^2}{\sigma_{ki}^{(0)3}}\epsilon_{ki}\sigma_{ki}^3\left(12\rho_{ki}^{13} - 6\rho_{ki}^7\right)\left[\frac{(\hat{\mu}_k\cdot\hat{r}_{ki} + \hat{\mu}_i\cdot\hat{r}_{ki})^2}{(1+\chi\hat{\mu}_k\cdot\hat{\mu}_i)^2} - \frac{(\hat{\mu}_k\cdot\hat{r}_{ki} - \hat{\mu}_i\cdot\hat{r}_{ki})^2}{(1-\chi\hat{\mu}_k\cdot\hat{\mu}_i)^2}\right]\right]\\
&+ 2\left(\hat{r}_{ki,\alpha} - \hat{\mu}_{k,\alpha}\hat{\mu}_k\cdot\hat{r}_{ki}\right)\left[\frac{\chi}{\sigma_{ki}^{(0)3}}\epsilon_{ki}\sigma_{ki}^3\left(12\rho_{ki}^{13} - 6\rho_{ki}^7\right)\right.\\
&\cdot\left[\frac{\hat{\mu}_k\cdot\hat{r}_{ki} + \hat{\mu}_i\cdot\hat{r}_{ki}}{1+\chi\hat{\mu}_k\cdot\hat{\mu}_i} + \frac{\hat{\mu}_k\cdot\hat{r}_{ki} - \hat{\mu}_i\cdot\hat{r}_{ki}}{1-\chi\hat{\mu}_k\cdot\hat{\mu}_i}\right]\\
&\left.\left.- \mu\chi'\frac{\varphi_{ki}}{\Theta_{ki}}\left[\frac{\hat{\mu}_k\cdot\hat{r}_{ki} + \hat{\mu}_i\cdot\hat{r}_{ki}}{1+\chi'\hat{\mu}_k\cdot\hat{\mu}_i} + \frac{\hat{\mu}_k\cdot\hat{r}_{ki} - \hat{\mu}_i\cdot\hat{r}_{ki}}{1-\chi'\hat{\mu}_k\cdot\hat{\mu}_i}\right]\right]\right\}
\end{aligned} \tag{32}
$$

Calculations have been carried out for 100 molecules and for simulation times up to $\delta t = 1$ fs. We considered that the molecules are bonded by the $CH=CH_2$ groups located at their extremity as represented in figure 19. The bonding of the molecules (the polymerization) takes

Figure 19. Schematical representation of the modeled elastomer.

place in such a way to produce a form of sheathing around the principal chain. Crosslinking between principal chains was modeled by resorting to alkyne chains.

To measure the contraction of the simulated system we have monitored the obtained dimensions of the simulation cell vectors L_x and L_y. In figure 20 and 21 we have represented the results of the simulation and the measured contraction. We can notice a difference between the curvature of the two curves.   Figure 22 represents the behavior of the order parameter
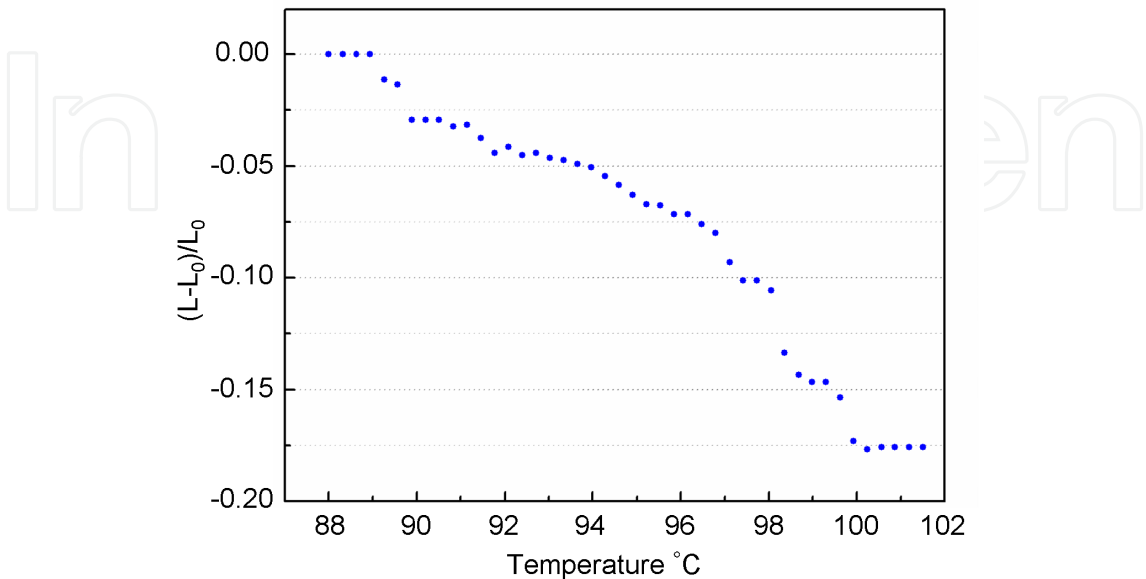

Figure 20. Contraction of the elastomer: fractional change in length $(L - L_0)/L_0$ as a function of temperature.
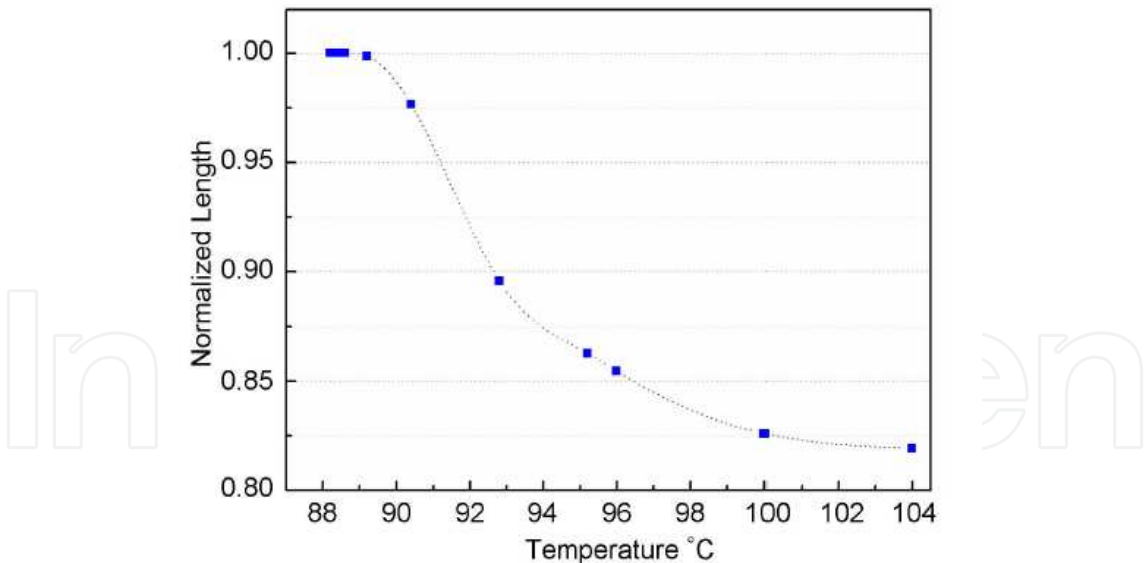

Figure 21. Simulation result. The curve is a guide to the eye.

obtained by polarized Fourier transform spectroscopy (FTIR) in the case of the same elastomer [45]. If we compare the simulation curve with figure 22 we can see that they have the same apparence. This similarity was to be expected, in fact it is the decrease of the order parameter which generates the contraction of the material. But differences between the behavior of the order parameter and the contraction can be identified: the contraction is not immediate, it
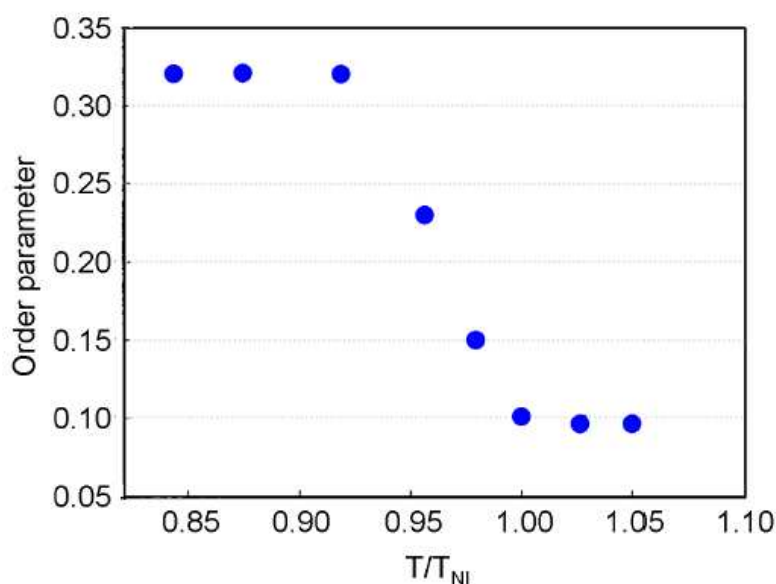
Figure 22. Order parameter as a function of reduced temperature T/T_{NI}, T_{NI} is the phase transition temperature [45].

starts above a given temperature which is higher than the phase transition temperature. In reality a sufficient contraction force should be achieved before observing the phenomena and these contraction forces should also exceed the friction forces with the glass plate. The fact that the simulation curve looks like the order parameter curve more than the contraction curve encourages us to consider external mechanical forces acting on the elastomer in the future.

6. Conclusion

We have demonstrated that one photon "UV" photopolymerization as well as two-photon "IR" photopolymerization can be used to microstructure artificial muscle materials made of nematic liquid crystalline elastomers without losing the contraction/extension properties. We have shown that the use of two-photon absorption allows to achieve 65 % greater spatial resolutions. A major advantage of the TPA consists in creating shape-changing volume objects, a property particularly interesting for the domain of microfluidics. We have established the possibility of generating a grating design in the sample which can be used as a step changing grating when subject to a temperature increase. We have shown that the contraction induced by the temperature is easily monitored by the widening of the diffraction figure. We can then consider the use of this kind of grating for temperature adjusted feedback devices. In addition, the birefringence properties of the gratings can open the path for polarization dependent diffractive elements.

Molecular dynamics simulations have been used to describe the contraction of the elastomer as a function of temperature. The proposed model allows the simulation of anisotropic molecules made from a combination of Gay-Berne potentials, representing the rigid mesogenic parts, and Lennard-Jones sites representing the alkyne groups of the flexible chains. Even if experimental and numerical contractions behave somewhat differently as functions of the temperature, a fact that may be attributed in part to the neglect of external

mechanical forces, a rather good agreement between the behavior of the simulation curve and the order parameter has been achieved and a reasonable agreement with the contraction curve has been obtained.

Author details

Kokou D. (Honorat) Dorkenoo, Hervé Bulou, Grégory Taupier, and Alex Boeglin
IPCMS, UMR 7504, 23 rue du Loess, BP 43, F-67034 Strasbourg Cedex 2, France

Emel Sungur
Bilkent University, Department of Physics, Advanced Research Laboratories, 06800, Ankara, Turkey

7. References

[1] Ikeda, T. and Tsutsumi, O. (1995) Optical switching and image storage by means of azobenzene liquid-crystal films. Science 268: 1873–1875.

[2] Lagerwall, S. T. (1999) Ferroelectric and Antiferroelectric Liquid Crystals. Wiley-VCH.

[3] Drzaic, P. S. (1999) Liquid Crystal Dispersions. World Scientific.

[4] Warner, M. and Terentjev, E.M. (2003) Liquid crystal elastomers. Oxford University Press, USA.

[5] de Gennes, P.G. (1997) A semi-fast artificial muscle. CR Acad. Sci. Ser. II B 324: 343-348.

[6] Yu, Y. and Ikeda, T. (2006) Two-Photon Excitation in CaF2Eu2+. Phys. Rev. Lett. 45: 5416-5418.

[7] Naciri, J. and Srinivasan, A. and Jeon, H. and Nikolov, N. and Keller, P. and Ratna, B.R. (2003) Nematic elastomer fiber actuator. Macromolecules 36: 8499-8505.

[8] Ikeda Y. Yu T., and Mamiya J.(2007) Soft actuators based on liquid-crystalline elastomers. Angaw. Chem. Int. Ed, 46: 506.

[9] De Gennes, P.G(1975) Réflexions sur un type de polymères nématiques. ACR Acad. Sci. Paris, Ser. B, 46: 101-103.

[10] Kupfer, J. and Finkelmann, H. (1991) Nematic liquid single crystal elastomers. Makromol Chem., Rapid Commun. 12: 717-726.

[11] Lessard, R. A. Gurusamy, M. (1995) Photoreactive Polymers in Advance Applications. Chapman and Hall, New York.

[12] McCammon, J.A. and Gelin, B.R. and Karplus, M. (1977) Dynamics of folded proteins. Nature. 267: 585–590.

[13] Allen, M.P. and Warren, M.A. and Wilson, M.R. and Sauron, A. and Smith, W. (1996) Molecular dynamics calculation of elastic constants in Gay-Berne nematic liquid crystals. J. Chem. Phys. 105: 2850-2858.

[14] Darinskii, A.A. and Zarembo, A. and Balabaev, N.K. (2007) Molecular Dynamic Simulation of Side-Chain Liquid Crystalline Elastomer Under Load. Macromolecular Symposia. 252: 101-109.

[15] Osada, Y. and Okuzaki, H. and Hori, H.(1992) A polymer gel with electrically driven motility. Nature 355: 242-244.

[16] Osada, Y. and De Rossi, D.E.(2000)Polymer sensors and actuators. Springer Berlin.

[17] Osada, Y. and Khokhlov, A.R. (2002)Polymer Gels and Networks. Marcel Dekker, Inc, 270 Madison Avenue, New York, NY 10016, USA, 1-381.

[18] Osada, Y. and Khokhlov, A.R. (1996)Conducting polymer artificial muscles. Synth. Met. 78: 339-354.

[19] Lu, W. and Fadeev, A.G. and Qi, B. and Smela, E. and Mattes, B.R. and Ding, J. and Spinks, G.M. and Mazurkiewicz, J. and Zhou, D. and Wallace, G.G. and others (2002)Use of ionic liquids for pi-conjugated polymer electrochemical devices. Science 297: 983.

[20] Pyo, M. and Bohn, C.C. and Smela, E. and Reynolds, J.R. and Brennan, A.B.(2003)Direct strain measurement of polypyrrole actuators controlled by the polymer/gold interface. Chem. Mater. 15: 916-922.

[21] Baughman, R.H. and Cui, C. and Zakhidov, A.A. and Iqbal, Z. and Barisci, J.N. and Spinks, G.M. and Wallace, G.G. and Mazzoldi, A. and De Rossi, D. and Rinzler, A.G. and others(1999)Carbon nanotube actuators. Science 284: 1340.

[22] Kim, P. and Lieber, C.M.(1999)Nanotube nanotweezers. Science 286: 2148.

[23] Zhang, Y. and Iijima, S.(1999) Elastic response of carbon nanotube bundles to visible light. Phys. Rev. Lett. 82: 3472-3475.

[24] Spinks, G.M. and Wallace, G.G. and Fifield, L.S. and Dalton, L.R. and Mazzoldi, A. and De Rossi, D. and Khayrullin, I.I. and Baughman, R.H.(2002) Pneumatic carbon nanotube actuators. Adv. Mater. 14: 1728-1732.

[25] KPelrine, R. and Kornbluh, R. and Pei, Q. and Joseph, J.(2000)High-speed electrically actuated elastomers with strain greater than 100%. Science 287: 836.

[26] Finkelmann, H. Kock, H.J. and Rehage, G.(1981)Investigations on liquid crystalline polysiloxanes 3. Liquid crystalline elastomers-a new type of liquid crystalline material. Makromol. Chem., Rapid Commun. 2: 317-322.

[27] Bergmann, G.H.F. and Finkelmann, H. and Percec, V. and Zhao, M.(1997) Liquid-crystalline main-chain elastomers. Macromol. Rapid Commun. 18: 353-360.

[28] C. Zannoni (1979) The molecular physics of liquid crystals. Rijeka: G. R. Luckhurst and G. W. Gray.

[29] Thomsen, D.L. and Keller, P. and Naciri, J. and Pink, R. and Jeon, H. and Shenoy, D. and Ratna, B.R.(2001)Liquid crystal elastomers with mechanical properties of a muscle. Macromolecules 34: 5868-5875.

[30] Zipfel, W.R. and Williams, R.M. and Webb, W.W.(2003)Nonlinear magic: multiphoton microscopy in the biosciences. Nature Biotechnology 21: 1369-1377.

[31] Zipfel, Naydenova, I. and Mihaylova, E. and Martin, S. and Toal, V.(2005) Holographic patterning of acrylamide–based photopolymer surface. Opt. Express 13: 4878-4889.

[32] Becke, A.D.(1993)Density-functional thermochemistry. III. The role of exact exchange. Chem. Phys. 98: 5648–5652.

[33] Valiev, M. and Bylaska,E.J. and Govind, N. and Kowalski, K. and Straatsma, T.P. and van Dam, H.J.J. and Wang, D. and Nieplocha, J. and Apra, E. and Windus, T.L. and de Jong, W.A.(2010) NWChem: a comprehensive and scalable open-source solution for large scale molecular simulations. Comput. Phys. Commun. 181: 1477.

[34] Gay, J.G. and Berne, B.J.(1981) Modification of the overlap potential to mimic a linear site–site potential. J. Chem. Phys. 74: 3316.

[35] Miguel, E. and Rull, L.F. and Chalam, M.K. and Gubbins, K.E. and Van Swol, F.(1991) Location of the isotropic-nematic transition in the Gay-Berne model. Mol. Phys. 72: 593-605.

[36] Luckhurst, G.R. and Stephens, R.A. and Phippen, R.W.(1990) Computer simulation studies of anisotropic systems. XIX. Mesophases formed by the Gay-Berne model mesogen. Liq. Cryst. 8: 451.

[37] Allen M. P., M. A. Warren, M. R. Wilson, A. Sauraon, and w. Smith(1996) molecular dynamics calculation of elastic constants in Gay-Berne nematic crystals. J. Chem. Phys. 105: 2850-2858.

[38] Rappe, AK and Casewit, CJ and Colwell, KS and Goddard Iii, WA and Skiff, WM (1999) UFF, UFF, a full periodic table force field for molecular mechanics and molecular dynamics simulations. JOSA 114: 10024-10035.

[39] Allen M. P., M. A. Warren, M. R. Wilson, A. Sauraon, and w. Smith(1985) molecular dynamics calculation of elastic constants in Gay-Berne nematic crystals. Mol. Phys. 55: 549.

[40] Cleaver, D.J. and Care, C.M. and Allen, M.P. and Neal, M.P.(1996) Extension and generalization of the Gay-Berne potential. Phys. Rev. E 54: 559-567.

[41] Parrinello, M. and Rahman, A.(1981) Polymorphic transitions in single crystals: A new molecular dynamics method. J. Appl. Phys. 52: 7182.

[42] Nose, S.(1984) A unified formulation of the constant temperature molecular dynamics methods. J. Chem. Phys. 81: 511.

[43] Hoover, W.G.(1985) Canonical dynamics: Equilibrium phase-space distributions. Phys. Rev. A 31: 1695-1697.

[44] Beeman, D.(1976) Some multistep methods for use in molecular dynamics calculations. J. Comput. Phys. 20: 130.

[45] Li, M.H. and Keller, P. and Li, B. and Wang, X. and Brunet, M.(2003) Light-driven side-on nematic elastomer actuators. Adv. Mater. E 15: 5569-572.